Nonintrusive Characterization Method for Integrated Optical Delay Lines

Pablo Martínez-Carrasco, Tan Huy-Ho, and Jose Capmany, *Fellow, IEEE*

***Abstract*—In this work we present an automatic calibration technique for switched Optical True Time Delay Lines which allows the control of all of the switchers without relaying on intermediate attenuators nor external test ports, thus optimizing the number of active elements on chip and the footprint. This technique has been used for the characterization of a delay line fabricated on a silicon photonic chip.The accuracy and reliability of this technique were validated for applications beyond beamforming by utilizing the calibration data to synthesize variable optical interleavers.**

***Index Terms*—Beamforming networks, microwave photonics, optical filters, silicon photonics, true time delay.**

I. Introduction and Context

IN RECENT years, microwave photonics has emerged as a technology with immense potential, destined to enhance the capacity and speed of modern telecommunications. This is especially critical in light of the escalating demands for high-speed and high-capacity communication driven by emerging applications like the Internet of Things (IoT) and future 5/6G networks [1], [2].

It accomplishes this by transcending the limitations of radiofrequency devices and systems, capitalizing on the unique optical attributes of low loss, minimal power consumption, broadband operation, immunity to electromagnetic interference, and extensive tunability [3]. This is achieved through the up-conversion of radiofrequency signals into the optical domain, their processing, and subsequent downconversion, effectively capitalizing on the advantages of photonics.

An area of substantial focus is optical true-time delay (OTTD), a technology enabling precise control over the propagation delay of optical signals. This capability finds application in various domains, including synchronization and buffering of optical signals [4], optical signal filtering and processing [5], and more recently, in reservoir computing [6].

Manuscript received 10 January 2024; revised 26 February 2024; accepted 14 March 2024. Date of publication 22 March 2024; date of current version 16 July 2024. This work was supported by Huawei under Contract YB20200065124. *(Corresponding author: Pablo Martínez-Carrasco.)*

Pablo Martínez-Carrasco and Jose Capmany are with Photonics Research Labs, iTEAM Research Institute, Universitat Politècnica de València, 46022 València, Spain (e-mail: pmarrom@iteam.upv.es; jcapmany@iteam.upv.es).

Tan Huy-Ho is with Ottawa Wireless Advanced System Competency Centre, Huawei Technologies Canada Company, Ottawa, ON K2K 3J1, Canada (e-mail: tan.ho@huawei.com).

Color versions of one or more figures in this article are available at https://doi.org/10.1109/JLT.2024.3380637.

Digital Object Identifier 10.1109/JLT.2024.3380637

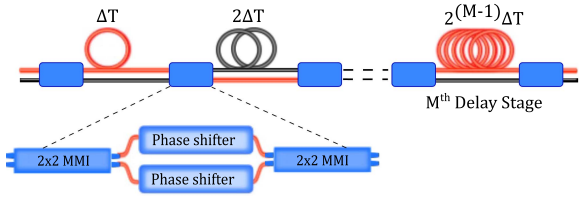

Fig. 1. Scheme of a single M-bit switched OTTDL, where ΔT is the basic delay of the line.

However, among these applications, OTTD has proven to be an ideal solution for phase array antennas (PAA) and beamforming networks, greatly enhancing their performance [7], [8]. These notable improvements over traditional beamformers stem from the elimination of the beam squint effect associated with electronic phase shifters, where changes in the microwave frequency cause a deviation in the pointing angle, limiting the operating bandwidth to less than a few hundred megahertz [9], [10], [11]. This translates into higher bandwidth, increased speed, and reduced power consumption.

The ongoing progress in integrated photonics has made it possible to integrate on-chip OTTD systems with increasingly complex circuits. This integration not only encompasses all the previously mentioned advantages but also extends to devices with an exceptionally compact footprint [12], [13]. Numerous schemes for implementing OTTD have been demonstrated, but among them, tunable OTTD based on microring resonators (MRRs) and optical switchable waveguides stand out for their simplicity and suitability for monolithic integration on silicon-on-insulator (SOI) chips.

PAA architectures relying on single and cascaded MRRs offer continuous time delay tuning, delivering high angular resolution [14], [15], [16], [17]. However, they encounter bandwidth limitations due to the resonant behavior of their delays and exhibit high sensitivity to thermal crosstalk and manufacturing errors. Conversely, switched delay lines, while offering a more limited angular resolution, provide significant operational bandwidth and exhibit low sensitivity to thermal effects and manufacturing variations, which make them the central focus of this work.

The uses of this type of integrated structures go beyond just PAA with high performance [18], [19], [20], [21], including wavelength division multiplexing (WDM) filters [22], [23], gain and dispersion equalization filters [24].

Fig. 1 depicts the conventional setup of a switched OTTDL. This configuration comprises *M* delay stages (bits) featuring two

selectable paths. The lower path maintains a constant length for each bit, while the other one exponentially increases its length as the number of bits progresses. These delay lines are interconnected by tunable switches, consisting of 2×2 Mach-Zehnder Interferometers (MZIs). By switching between the long and short delay paths in each stage, it is possible to achieve discrete delays that are multiples of a fundamental delay ΔT, from 0 to $(2^M - 1)\Delta T$. This method of obtaining delays can be straightforwardly represented using binary notation, where a "0" denotes the selection of a short path in a delay stage, and a "1" represents the selection of a long path.

In this scheme, it is customary to incorporate variable optical attenuators (VOAs) [18], [19], [21] or test ports (such as photodetectors or grating couplers) [20] between the delay stages. These elements are strategically placed along all connection waveguides, serving two objectives. Firstly, they enable the calibration of the optical switches, ensuring accurate switching states. Secondly, they attenuate the residual signal in the case of having limited extinction ratio (ER) on the switches, thereby enhancing the quality of the transmitted signal. However, both configurations introduce additional complexity to the integrated circuit, accompanied by higher power consumption due to the VOAs and extra insertion losses caused by the test ports. Most notably, these additions result in an increase of the chip's footprint and more complex packaging.

Non-invasive characterization techniques have recently been studied in the literature, such as using intermediate phase shifters in the delay stages as monitoring elements that avoid adding losses [25], or techniques that rely on optimization algorithms to reduce the standard deviation in the optical response of the delay lines [26].

In this paper, we extend the work presented in [27], and we present and validate a calibration method for switched delay lines that eliminates the necessity of supplementary structures. Our proposed approach allows for the development of novel architectures that are not only more compact but also exhibit reduced power consumption. Section II introduces the calibration method based on spectral Fourier transform. In Section III, we show the details of the silicon photonic OTTDL used for the experimental demonstration of the proposed approach. Moving forward, Section IV discusses the chip calibration measurements and demonstrates its application for a tunable optical interleaver based on a lattice filter, showcasing the method's efficacy. Finally, in Section V, we provide a summary and conclusions of the study.

II. Calibration Method

While theoretically, the initial state of each MZI should be a perfect cross-state, this ideal state is often far from reality. Minor variations in the width and height of the waveguides in the two paths of the MZI result in discrepancies in the group index, leading to a phase difference between the arms. Typically, the default state of each MZI in the OTTDL is unpredictable and random due to these manufacturing imperfections and that is the reason of using VOAs or test ports. Nonetheless, we present an alternative approach that only utilizes Fourier transform analysis of the optical spectrum.

Equation (1) characterizes the transfer function of an individual tunable coupler, expressed as a function of the phase ϕ applied to one of its arms.

$$H_{TC}(\phi) = -ie^{i(\phi/2)} \begin{bmatrix} \sin(\phi/2) & \cos(\phi/2) \\ \cos(\phi/2) & -\sin(\phi/2) \end{bmatrix} \tag{1}$$

The phase variation is uniform across both outputs and will be eliminated post-photodetection, rendering it inconsequential. Given this, we can simplify the preceding equation by expressing it in terms of the coupling coefficient κ.

$$H_{TC}(\kappa) = \begin{bmatrix} s(\kappa) & c(\kappa) \\ c(\kappa) & -s(\kappa) \end{bmatrix} = \begin{bmatrix} \sqrt{1-\kappa} & \sqrt{\kappa} \\ \sqrt{\kappa} & -\sqrt{1-\kappa} \end{bmatrix} \tag{2}$$

When a signal is injected into one of the inputs of the delay line, the initial tunable switch divides the signal between the paths of the first delay stage and the subsequent tunable coupler combine them.

$$\begin{aligned} H_{DS} &= H_{TC}(\kappa_1) H_{Delay} H_{TC}(\kappa_0) \\ &= \begin{bmatrix} s_1 & c_1 \\ c_1 & -s_1 \end{bmatrix} \begin{bmatrix} e^{i\omega\Delta T} & 0 \\ 0 & 1 \end{bmatrix} \begin{bmatrix} s_0 & c_0 \\ c_0 & -s_0 \end{bmatrix} \\ &= \begin{bmatrix} s_0 s_1 e^{i\omega\Delta T} + c_0 c_1 & c_0 s_1 e^{i\omega\Delta T} - s_0 c_1 \\ s_0 c_1 e^{i\omega\Delta T} - c_0 s_1 & c_0 c_1 e^{i\omega\Delta T} + s_0 s_1 \end{bmatrix} \end{aligned} \tag{3}$$

The time difference between paths is related with the physical length difference, ΔL, and the group index, n_g, of the waveguide mode, $\Delta T = n_g \Delta L / c$.

This analysis can be extended for additional tunable couplers and delay stages and after photodetection, the contributions from all length imbalances mix in the photodiode. Hence, in the presence of optical leakages between delay stages resulting from inefficient switching, we will detect a distinctive interferometric pattern in the frequency response of the delay line. This pattern exhibits a combination of all the characteristic Free Spectral Range (FSRs) corresponding to all the length imbalances across each delay stage and the associated coupling coefficients.

To illustrate the calibration procedure, consider a generic switched OTTDL with 3 delay stages with respective delay values of ΔT, $2\Delta T$ and $4\Delta T$. The transfer matrix of the delay line has been calculated similarly to the one expressed in (3), but with the inclusion of two additional delay stages alternated between tunable couplers. Equation (4) shown at the bottom of the next page, depicts the photodetected normalized optical power considering a bar-state transmission at the top port, $|H_{11}|^2$, the signal is injected through the top input, and the measurement is taken at the top output.

The frequency-dependent nature of the response creates a periodic pattern. Only relying on the spectrum is insufficient for accurately characterizing the MZIs; it is necessary to take the Fourier transform. By doing so we move from frequency to time space, in other words, to a space in which the repeating patterns in the spectrum are quantified. One of the benefits of using the Fourier Transform is its independence from the absolute optical

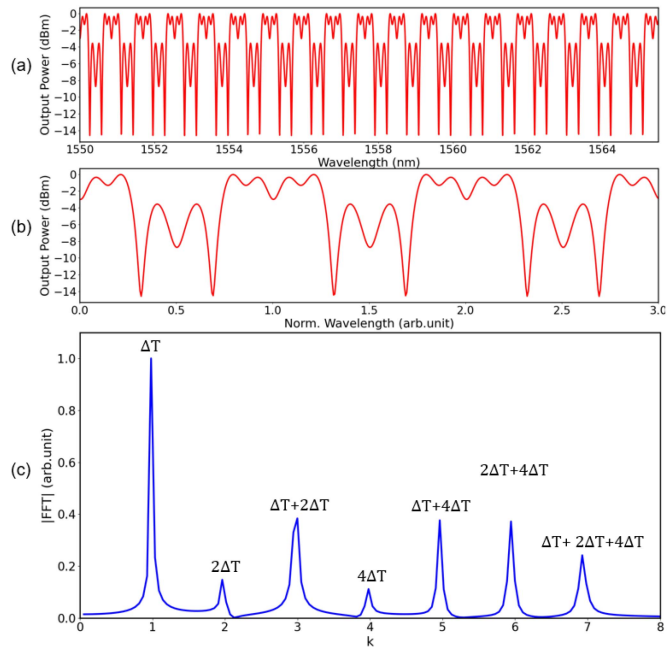

Fig. 2. (a) Optical spectrum of a random state in the OTTDL example. (b) Zoom of a section of the spectrum normalized to the largest FSR, covering 3 repetitions. (c) Fourier transform of the spectrum through the OTTDL expressed as a function of all the possible time combinations.

power measured; only a relative measurement is needed. This is because the information provided by the FFT relies exclusively on the shape of the spectrum, not its absolute power. As shown in (5) shown at the bottom of the next page, the Fourier transform exhibits peaks in time aligning with the inverse of the FSRs associated with the different delay interferences. Thus, each peak contains information about the 'intensity' in the number of repetitions in the spectrum corresponding to the different time combinations. Fig. 2 represents the optical response for a random configuration of this delay line. With the transformed spectrum we are able to discern the contributions of the different optical paths and to know which MZIs are in an intermediate state.

Since all time differences in the delay stages are multiples of a fundamental basic delay, we can normalize the time to this value, $k = t/\Delta T$. That way the peaks will be located uniformly as shown in Fig. 2(c).

Algorithm 1: Delay Line Calibration.

Stage 1: Characterize the first M MZIs
for $i = 1$ to M **do**
  Sweep current applied to MZI$_i$
    With $u \in \{n | n \in \mathbb{N}, 1 \leq n \leq 2^{(M-i)}, n \text{ odd}\}$
    Save first current that nulls the peaks $2^{(i-1)}u\Delta T$
    Save second current that nulls the peak $2^{(i-1)}u\Delta T$
  Apply first/second current to MZI$_i$
end for
Stage 2: Characterize the last MZI
Sweep current applied to MZI$_{M+1}$
  Save current that maximizes the output optical power
  Save current that minimizes the output optical power

By systematically adjusting the currents from the first MZI to the latest one, we can effectively suppress the contributions on the spectrum. This process involves gradually diminishing the peaks of interference on the transformed spectrum, starting with those associated with the smallest optical delays.

We commence the tuning process with the first MZI. Referring to (5), it becomes evident that the initial peak cancellation occurs only when this MZI is in either the bar state ($s_0 = 1$ and $c_0 = 0$) or the cross state ($s_0 = 0$ and $c_0 = 1$). By doing this, we not only suppress the first interference peak but also eliminate all odd contributions, as they all share a common factor of $s_0 c_0$.

Then, we repeat the same process with the second MZI, shutting down the peak corresponding to $2\Delta T$ when $s_1 = 0$ or $c_1 = 0$. At this point, the peak corresponding to $6\Delta T$ will also have vanished, leaving only the contribution of the third delay stage. We perform the same procedure once more for s_2 and c_2, suppressing the peak at $4\Delta T$. Subsequently, we determine the bar and cross states of the final MZI by optimizing the optical power, adjusting s_3 and c_3. Algorithm 1 shows a more detailed version of this process for a delay line with M delay stages, $(M+1)$ MZIs.

Finally, when the spectrum has been completely flattened, it indicates that all the MZIs have reached either a perfect bar or cross state, this is $\kappa_n \in \{0, 1\}$. At this point, the remaining question is to determine which specific state each MZI is in. To accomplish this, we can utilize a Vector Network Analyzer (VNA) to measure the phase of the signal and extract the corresponding delay information.

$$
\begin{aligned}
P_0(\omega) = {} & (s_0 s_1 s_2 s_3)^2 + (s_0 s_1 c_2 c_3)^2 + (c_0 c_1 s_2 s_3)^2 + (c_0 c_1 c_2 c_3)^2 + (s_0 c_1 c_2 s_3)^2 + (s_0 c_1 s_2 c_3)^2 + (c_0 s_1 c_2 s_3)^2 \\
& + (c_0 s_1 s_2 c_3)^2 + 2 s_0 c_0 \left[s_1 c_1 \left((s_2 s_3)^2 + (c_2 c_3)^2 - (s_2 c_3)^2 - (c_2 s_3)^2 \right) + c_1^2 s_2 c_2 \left(s_3^2 - c_3^2 \right) - s_1^2 c_2^2 s_3 c_3 \right] \cos(\omega \Delta T) \\
& + 2 s_1 c_1 c_2 \left[s_2 \left((s_0 s_3)^2 + (c_0 c_3)^2 - (s_0 c_3)^2 - (c_0 s_3)^2 \right) + c_2 s_3 c_3 \left(s_0^2 - c_0^2 \right) \right] \cos(\omega 2 \Delta T) \\
& + 2 s_0 c_0 c_2 \left[s_3 c_3 \left(2 s_1 c_1 s_2 + c_1^2 c_2 \right) + s_1^2 s_2 \left(c_3^2 - s_3^2 \right) \right] \cos(\omega 3 \Delta T) \\
& + 2 s_2 c_2 s_3 c_3 \left[(s_0 s_1)^2 + (c_0 c_1)^2 - (s_0 c_1)^2 - (c_0 s_1)^2 \right] \cos(\omega 4 \Delta T) \\
& + 2 s_0 c_0 c_1 s_2 s_3 c_3 \left[2 s_1 c_2 - c_1 s_2 \right] \cos(\omega 5 \Delta T) + 2 s_1 c_1 s_2^2 s_3 c_3 \left[s_0^2 - c_0^2 \right] \cos(\omega 6 \Delta T) + 2 s_0 c_0 s_1^2 s_2^2 s_3 c_3 \cos(\omega 7 \Delta T) \quad (4)
\end{aligned}
$$

III. Chip Structure

In order to evaluate the characterization method, an OTTDL was specifically designed for use as a reconfigurable lattice filter. The OTTDL configuration consists of 5 delay stages and 6 tunable couplers. The unit delay within the system has a value of $\Delta T = 9.5$ ps, resulting in a maximum delay of $16\Delta T = 152$ ps for the final stage.

The photonic integrated circuit was produced by Advanced Micro Foundry, using a conventional Silicon-on-Insulator (SoI) fabrication process. The chip was crafted from an SoI wafer with a 220 nm thick slab, and deep ultraviolet lithography (193 nm) was employed to define the 500 nm wide single-mode waveguides.

For the waveguide sections containing phase shifters, a thin heater layer consisting of 120 nm TiN was deposited over the waveguide, which is powered by metal DC tracks of 2000 nm thickness. These thermo-optic phase actuators are implemented using suspended waveguides and trenches, key elements that enable a reduced power consumption of only 1.35 mW/π. Fig. 4 shows the layout and the micrograph of the fabricated silicon photonics OTTDL.

IV. Experimental Results

A. Experimental Calibration

The calibration process was executed according to the technique described in Section II. The chip was powered through a multicontact probe equipped with 8 electrical channels, and optical input and output were facilitated using a single fiber and grating couplers. For the wavelength sweep, we employed a tunable laser, the EXFO T100S-HP, in conjunction with a full-band component tester, the EXFO CT440 comb source. The wavelength span we utilized was 3 nm, with a resolution of 1 pm. Smaller delay lengths may necessitate larger spans to achieve the highest resolution in the reciprocal spectrum.

Fig. 3 illustrates the characterization process, presenting both the optical spectrum and its corresponding Fourier transform in a unified view.

At first, the line arrived with the MZIs in a completely random state (first row of Fig. 3) resulting in a spectrum with numerous interferences and contributions in time. We initiated the process by suppressing the first peak, which was all most negligible, until we saw how all the odd terms disappeared (second row of Fig. 3). As we systematically turned off contributions by configuring the MZIs in the bar or cross positions, the spectrum became smoother, and the contributions gradually vanished. This iterative process was repeated for the second and third MZIs, ultimately leaving us with only the contributions of the last two delay stages (third row of Fig. 3). Unfortunately, due to limited ER, thermal crosstalk, and electrical precision, achieving a fully flattened spectrum is impossible, resulting in small, uncorrelated noise variations in both frequency and time domains. In our experimental demonstration, the best result we achieved exhibited a standard deviation in the optical spectrum of 0.4 dB compared to the ideal value.

After achieving a this flattened optical spectrum, the next step involved measuring the phase and group delay for all the bar/cross configurations, thus 32 different positions. Utilizing a phase-shift approach, the RF-to-RF response was measured as the signal traveled through the integrated circuit, thereby providing information of the delay suffered by the signal for each line configuration. The input RF-modulated signal was generated by a VNA Agilent N5245 A capable of modulating signals up to 50 GHz. With a lightwave component analyzer (LCA) module N4373 C we upconverted the signals to the optical domain using a 1550 nm internal source. Afterwards, the output signal from the OTTDL was also downconverted using the same optical module from the VNA. The experimental setup is shown in Fig. 5(d).

Fig. 5 shows the phase, time, and optical response of the line across its 32 delay states. We extract the applied delay across a broad spectrum of frequencies from the RF phase measurements. Once we have all the delays ordered in ascending order, it becomes straightforward to correlate the set of currents applied for each delay with the bar or cross position of the MZIs.

In Fig. 5(c), the measured optical transmission response is depicted, with the power difference between bit configurations attributed to variations in propagation and bend losses across each stage. The obtained delay values exhibit minimal deviation from the theoretical delays, with an average discrepancy of only $\pm 0.16\,ps$, as shown in Fig. 6.

$$
\begin{aligned}
FTT(t) = & \int_{-\infty}^{\infty} P_0(\omega) e^{-i2\pi\omega t} d\omega \propto \\
& \propto s_0 c_0 \left[s_1 c_1 \left((s_2 s_3)^2 + (c_2 c_3)^2 - (s_2 c_3)^2 - (c_2 s_3)^2 \right) + c_1^2 s_2 c_2 \left(s_3^2 - c_3^2 \right) - s_1^2 c_2^2 s_3 c_3 \right] \delta(t \pm \Delta T) \\
& + s_1 c_1 c_2 \left[s_2 \left((s_0 s_3)^2 + (c_0 c_3)^2 - (s_0 c_3)^2 - (c_0 s_3)^2 \right) + c_2 s_3 c_3 \left(s_0^2 - c_0^2 \right) \right] \delta(t \pm 2\Delta T) \\
& + s_0 c_0 c_2 \left[s_3 c_3 \left(2 s_1 c_1 s_2 + c_1^2 c_2 \right) + s_1^2 s_2 \left(c_3^2 - s_3^2 \right) \right] \delta(t \pm 3\Delta T) \\
& + s_2 c_2 s_3 c_3 \left[(s_0 s_1)^2 + (c_0 c_1)^2 - (s_0 c_1)^2 - (c_0 s_1)^2 \right] \delta(t \pm 4\Delta T) \\
& + s_0 c_0 c_1 s_2 s_3 c_3 \left[2 s_1 c_2 - c_1 s_2 \right] \delta(t \pm 5\Delta T) + s_1 c_1 s_2^2 s_3 c_3 \left[s_0^2 - c_0^2 \right] \delta(t \pm 6\Delta T) + s_0 c_0 s_1^2 s_2^2 s_3 c_3 \delta(t \pm 7\Delta T) \quad (5)
\end{aligned}
$$

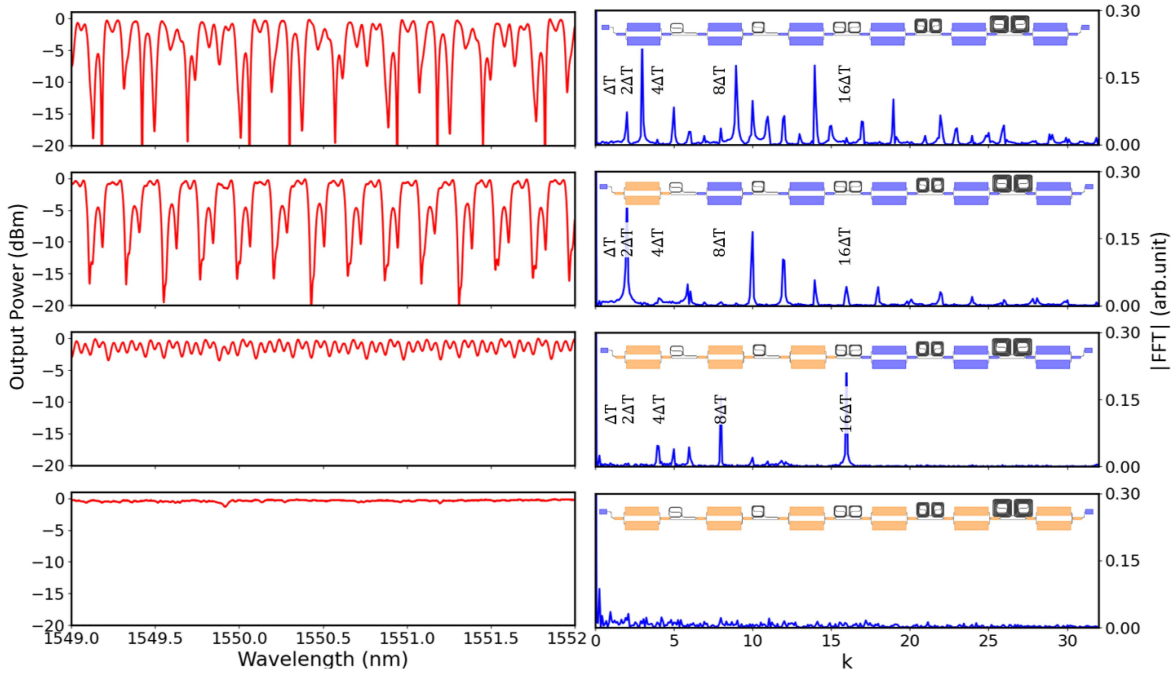

Fig. 3. Experimental measurements of OTTDL calibration. Each row in the figure shows the spectrum, its Fourier transform, and the corresponding configuration of the MZIs. The MZIs that remain in their original random state are highlighted in blue, while the ones in the bar/cross state are highlighted in orange. As the entire delay line transitions to the bar/cross state the spectrum becomes completely flat, devoid of any peaks in its transform.

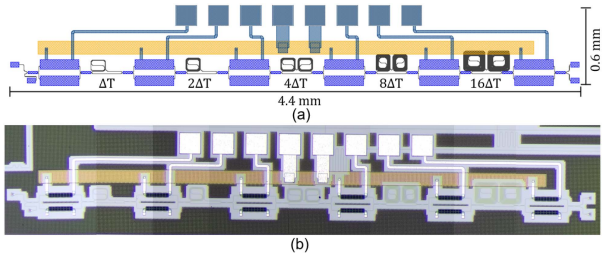

Fig. 4. Layout (a) and micrograph (b) of the fabricated silicon photonics OTTDL (4.4 mm × 0.6 mm).

Once we determine the precise locations of all the bar and cross states, we isolate each MZI one by one for independent characterization, as illustrated in Fig. 7. We consistently measure the bar transmission of the OTTDL, ensuring all MZIs are set to the bar state except for the one being characterized, whose current is going to be swept. Fig. 7(a) shows the characteristic curve of one of the MZIs of the line, demonstrating a large ER, an encouraging indication of the accurate outcome of the characterization method.

Utilizing these curves, we executed an adjustment of the coupling coefficient vs electrical current, $\kappa(I)$, a crucial step for the following synthesis of filters within the line. The fitting curve of the coupling coefficient can be obtained from (1) and (2). We compare both bar transmission terms for optical power, $|H_{11}|^2$, and fit them to the applied current, considering that the induced phase shift on the thermo-optic actuators follows a quadratic formula.

$$\kappa(I) = 1 - \sin^2\left(\alpha_0 + \alpha_1 I + \alpha_2 I^2\right) \tag{6}$$

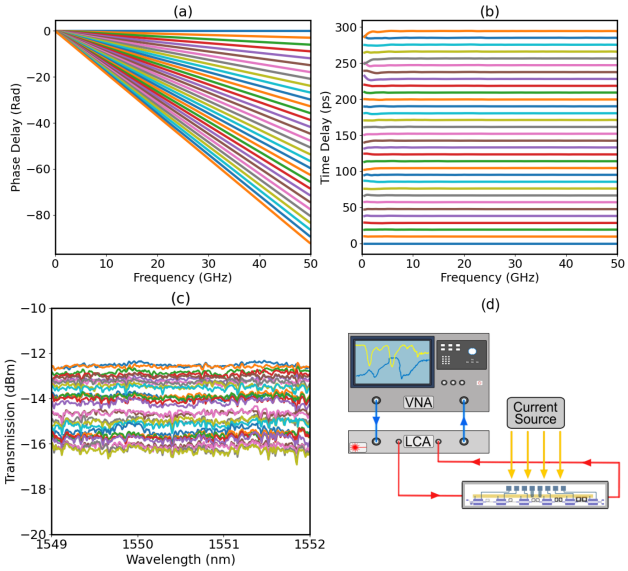

Fig. 5. (a) Microwave phase and (b) group delay responses for all 32 delay states of the OTTDL.(c) Transmission spectra for all bit configurations. (d) Experimental setup.

B. Application for Optical Filter Synthesis

We have adapted the synthesis of lattice-based filters developed in Madsen's work [28] to the simplified design of our OTTDL. This design, specifically tailored for beamforming applications, omits phase shifters between the delay stages, thereby limiting flexibility in terms of filtering design.

The following equations construct the transfer matrix after the n^{th} delay stage, where $c_n = \sqrt{1-\kappa_n}$, $s_n = \sqrt{\kappa_n}$

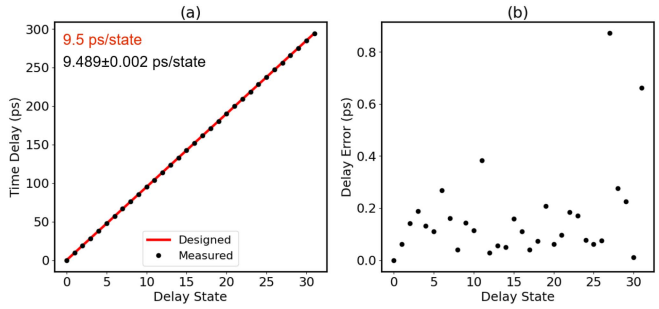

Fig. 6. (a) Delay measurement results using the calibration method compared with the designed values. (b) The delay time errors of 32 delay states.

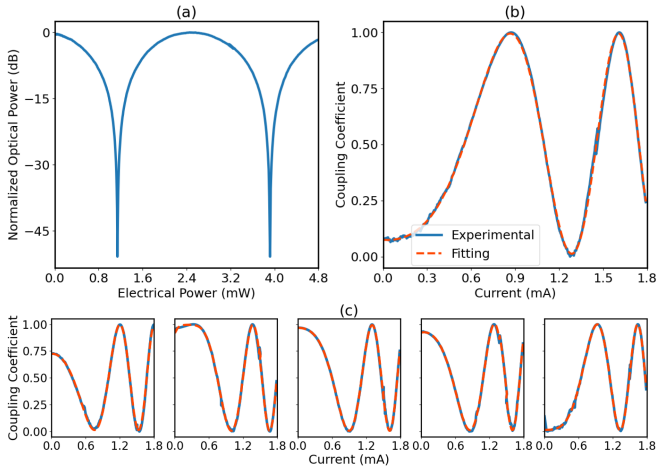

Fig. 7. (a) MZI transfer function depending on the electrical power applied on the thermo-optic actuator. (b) Coupling coefficient fit depending on the given current. (c) Fittings of all the MZIs in the line.

and $m = 2^{(n-1)}$.

$$\begin{bmatrix} X_n(z) \\ Y_n(z) \end{bmatrix} = \Phi_n(z) \begin{bmatrix} X_{n-1}(z) \\ Y_{n-1}(z) \end{bmatrix} \tag{7}$$

$$\Phi_n(z) = \begin{bmatrix} c_n & -is_n \\ -is_n & c_n \end{bmatrix} \begin{bmatrix} z^{-m} & 0 \\ 0 & 1 \end{bmatrix} \tag{8}$$

Iteratively applying the equations from a single delay stage to five, we derive the total transfer function in the Z-domain for our OTTDL.

$$\begin{bmatrix} X_{out}(z) \\ Y_{out}(z) \end{bmatrix} = \Phi_5\Phi_4\Phi_3\Phi_2\Phi_1\Phi_0 \begin{bmatrix} X_{in}(z) \\ Y_{in}(z) \end{bmatrix} \tag{9}$$

Then, we utilize an optimization algorithm based on standard minimization of the filter response in comparison to an ideal mask. This fine-tunes the couplings of the MZIs, ensuring that the final response aligns with a desired filter mask, within the design parameters if feasible.

The calculated coupling coefficients are then applied to the lattice filter making use of the previous characterization fittings. This enables us to synthesize interleavers that are based on notch and bandpass filters, shown in Fig. 8.

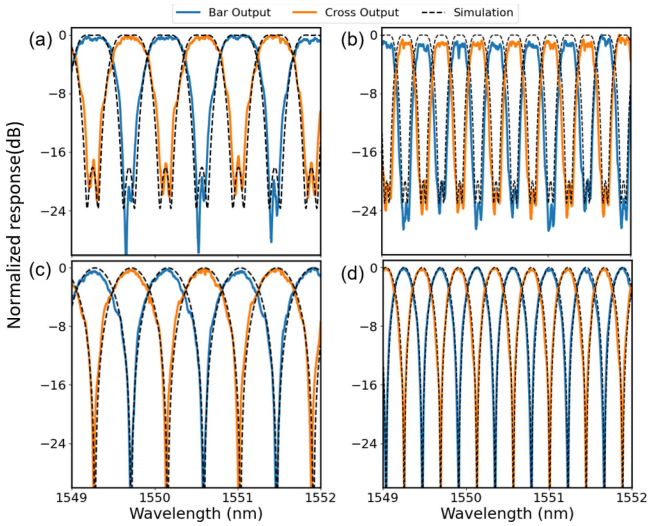

Fig. 8. (a) Measured bandpass filter with 52 GHz of bandwidth. (b) Measured bandpass filter with 26 GHz of bandwidth. (c) Measured notch filter with 106 GHz of FSR. (d) Measured notch filter with 53 GHz of FSR.

TABLE I
FILTER PARAMETERS

Filter	κ_0	κ_1	κ_2	κ_3	κ_4	κ_5
Bandpass (52 GHz)	0.5	0.6	0.04	0	0	0
Bandpass (26 GHz)	0	0.5	0.6	0.05	0.001	0
Notch (106 GHz)	0.5	0.5	0.002	0	0	0
Notch (53 GHz)	0	0.5	0.5	0.005	0	0

Table I presents the corresponding coupling coefficients for each filter. The results are very close to the theoretical values, demonstrating the accurate and precise performance of our proposed characterization method.

V. CONCLUSION

We have introduced a calibration method tailored for switched OTTDL, marking a significant advancement by eliminating the requirement for VOAs or dedicated test ports. This strategic elimination not only optimizes power consumption but also contributes to a more efficient utilization of device footprint. Through experimental validation, we have successfully demonstrated the efficacy of this calibration method on a silicon photonic chip. We successfully characterized an OTTDL and, leveraging the results obtained through this characterization, we extended the application to configure tunable optical interleavers. By introducing this approach, we pave the way for the development of more compact and simplified designs, addressing the critical need for miniaturization in next-generation communications technologies.

REFERENCES

[1] V. Jungnickel et al., "The role of small cells, coordinated multipoint, and massive MIMO in 5G," *IEEE Commun. Mag.*, vol. 52, no. 5, pp. 44–51, May 2014.

[2] C.-X. Wang et al., "Cellular architecture and key technologies for 5G wireless communication networks," *IEEE Commun. Mag.*, vol. 52, no. 2, pp. 122–130, Feb. 2014.

[3] J. Capmany and D. Novak, "Microwave photonics combines two worlds," *Nature Photon.*, vol. 1, no. 6, pp. 319–330, 2007.
[4] T. Alexoudi, G. T. Kanellos, and N. Pleros, "Optical RAM and integrated optical memories: A survey," *Light Sci. Appl.*, vol. 9, no. 1, 2020, Art. no. 91.
[5] J. Sancho et al., "Integrable microwave filter based on a photonic crystal delay line," *Nature Commun.*, vol. 3, no. 1, 2012, Art. no. 1075.
[6] K. Harkhoe, G. Verschaffelt, A. Katumba, P. Bienstman, and G. V. d. Sande, "Demonstrating delay-based reservoir computing using a compact photonic integrated chip," *Opt. Exp.*, vol. 28, no. 3, pp. 3086–3096, 2020.
[7] I. Frigyes and A. Seeds, "Optically generated true-time delay in phased-array antennas," *IEEE Trans. Microw. Theory Techn.*, vol. 43, no. 9, pp. 2378–2386, Sep. 1995.
[8] R. Rotman, M. Tur, and L. Yaron, "True time delay in phased arrays," *Proc. IEEE*, vol. 104, no. 3, pp. 504–518, Mar. 2016.
[9] P. Delos, B. Broughton, and J. Kraft, "Phased array antenna patterns—Part 2: Grating lobes and beam squint," *AnalogDialogue*, vol. 54, no. 2, pp. 1–4, 2020.
[10] M. E. Belkin, D. Fofanov, V. Golovin, Y. Tyschuk, and A. S. Sigov, "Design and optimization of photonics-based beamforming networks for ultra-wide mm wave-band antenna arrays," *Chapter*, vol. 4, pp. 47–67, 2018.
[11] R. L. Haupt, "Factors that define the bandwidth of a phased array antenna," in *Proc. IEEE Int. Symp. Phased Array Syst. Technol.*, 2019, pp. 1–4.
[12] D. Marpaung, J. Yao, and J. Capmany, "Integrated microwave photonics," *Nature Photon.*, vol. 13, no. 2, pp. 80–90, 2019.
[13] J. Yao, "Microwave photonics," *J. Lightw. Technol.*, vol. 27, no. 3, pp. 314–335, Feb. 2009.
[14] A. Meijerink et al., "Novel ring resonator-based integrated photonic beamformer for broadband phased array receive antennas–Part I: Design and performance analysis," *J. Lightw. Technol.*, vol. 28, no. 1, pp. 3–18, Jan. 2010.
[15] G. Lenz, B. Eggleton, C. K. Madsen, and R. Slusher, "Optical delay lines based on optical filters," *IEEE J. Quantum Electron.*, vol. 37, no. 4, pp. 525–532, Apr. 2001.
[16] C. Xiang, M. L. Davenport, J. B. Khurgin, P. A. Morton, and J. E. Bowers, "Low-loss continuously tunable optical true time delay based on Si3N4 ring resonators," *IEEE J. Sel. Topics Quantum Electron.*, vol. 24, no. 4, Jul.-Aug. 2018, Art. no. 5900109.
[17] Y. Liu et al., "Ultra-low-loss silicon nitride optical beamforming network for wideband wireless applications," *IEEE J. Sel. Topics Quantum Electron.*, vol. 24, no. 4, Jul.-Aug. 2018, Art. no. 8300410.
[18] J. Xie, L. Zhou, Z. Li, J. Wang, and J. Chen, "Seven-bit reconfigurable optical true time delay line based on silicon integration," *Opt. Exp.*, vol. 22, no. 19, pp. 22707–22715, Sep. 2014. [Online]. Available: https://opg.optica.org/oe/abstract.cfm?URI=oe-22-19-22707
[19] C. Zhu, L. Lu, W. Xu, G. Zhou, L. Zhou, and J. Chen, "Integrated 5-bit microwave photonic beamformer for broadband phased array antenna applications," in *Proc. 45th Eur. Conf. Opt. Commun.*, 2019, pp. 1–4.
[20] P. Zheng et al., "A seven bit silicon optical true time delay line for Ka-band phased array antenna," *IEEE Photon. J.*, vol. 11, no. 4, Aug. 2019, Art. no. 5501809.
[21] B. Pan, S. Zheng, C. Ren, X. Yu, and X. Zhang, "A structure optimization for integrated binary reconfigurable true time delay lines," *Opt. Commun.*, vol. 502, 2022, Art. no. 127439.
[22] F. Horst, W. M. Green, S. Assefa, S. M. Shank, Y. A. Vlasov, and B. J. Offrein, "Cascaded Mach-Zehnder wavelength filters in silicon photonics for low loss and flat pass-band WDM (de-) multiplexing," *Opt. Exp.*, vol. 21, no. 10, pp. 11652–11658, 2013.
[23] M. Kuznetsov, "Cascaded coupler Mach-Zehnder channel dropping filters for wavelength-division-multiplexed optical systems," *J. Lightw. Technol.*, vol. 12, no. 2, pp. 226–230, Feb. 1994.
[24] K. Takiguchi, K. Jinguji, K. Okamoto, and Y. Ohmori, "Variable group-delay dispersion equalizer using lattice-form programmable optical filter on planar lightwave circuit," *IEEE J. Sel. Topics Quantum Electron.*, vol. 2, no. 2, pp. 270–276, Jun. 1996.
[25] Z. Yang et al., "High accurate self-calibration of photonic integrated circuit using lossless thermo-optic phase shifters," *Opt. Exp.*, vol. 30, no. 26, pp. 47505–47514, 2022.
[26] S. Shi et al., "Non-invasive delay state calibration of silicon optical switching delay line," *J. Lightw. Technol.*, vol. 40, no. 19, pp. 6444–6453, Oct. 2022.
[27] P. MartÃ-nez-Carrasco, T. Huy-Ho, and J. Capmany, "Self-characterization method for integrated optical delay lines," in *Proc. Int. Topical Meeting Microw. Photon.*, 2023, pp. 1–4.
[28] C. K. Madsen and J. H. Zhao, *Optical Filter Design and Analysis*. New York, NY, USA: Wiley, 1999.

Pablo Martínez-Carrasco received the B.S. degrees in physics from the University of Valencia, Valencia, Spain, in 2020, and the M.S degree in telecommunication engineering from the Polytechnic University of Valencia, Valencia, in 2021. That year he joined the Photonics Research Labs where he is currently working toward the Ph.D. degree. His research interests include photonic integrated circuits and its applications to signal processing and computing, including optical communication systems and photonic beamforming architectures for wireless communications.

Tan Huy-Ho received the B.S. degree in EE from the University of Victoria, British CO, Canada, in 1996 and the M.S. degree (part-time) from Carleton University, Ottawa, ON, Canada, in 2014. He has been in the wireless and datacom industries for over 28 years working in various companies including start-up and established corporations such as Nortel Networks, Ciena Corporation, Spirent Communications, Ericsson Canada and has been with Huawei Technologies Canada since 2014. His current research interests include mmW/THz wireless system architecture and technologies, and microwave-photonics technologies for wireless integrated sensing and communications.

Jose Capmany (Fellow, IEEE) received the B.Sc., M.Sc. and Ph.D. degrees in telecommunications engineering and the B.Sc., M.Sc. and Ph.D. degrees in physics. Over the last 30 years he has been working in various areas of Photonics and Optical communications and his core expertise is in Microwave Photonics and Radio over Fiber Systems, but he is also interested in Quantum Communications and Integrated Optics. He has authored or coauhored more than 500 papers in international SCI ranked journals and Conferences. He is a Fellow of OSA and the IET. In 2012 he received the King James I Award in novel technologies, the highest scientific distinction in Spain, and he has recently been awarded with his second ERC Advanced Grant.